THE 2000 AIAA DRYDEN LECTURE

SPACE IMAGING RADAR IN PLANETARY EXPLORATION AND EARTH OBSERVATION

Charles Elachi
Jet Propulsion Laboratory/NASA
California Institute of Technology
Pasadena, California 91109

ABSTRACT

Spaceborne imaging radars are becoming key tools for mapping Earth and planetary surfaces, and near subsurface. Developments in the last decade are leading to capabilities for three dimensional surface imaging, detection of surface subtle motion due to earthquakes or volcanic activities, "color" mapping of surface properties, assessment of vegetation cover, etc... In planetary exploration, the radar capability to penetrate through cloud and haze cover, and possibility of sounding below the surface cover are providing a special perspective on the planetary surface and near surface evolution. This paper provides an overview of the techniques and technology of spaceborne imaging radars and their present and future potential applications.

I. INTRODUCTION

In June 1978, the Seasat satellite was put into orbit around the Earth with synthetic aperture-imaging radar (SAR) as one of the payload sensors [1]. The Seasat SAR provided, for the first time, synoptic radar images of the Earth's surface with a resolution of 25 m. The success of this complex sensor was a major technological advance, and it opened up a new dimension in our capability to observe, monitor, and study the Earth's surface [2], [3]. In November 1981, the second imaging radar was successfully operated from space on the shuttle [4]. The Shuttle Imaging Radar-A (SIR-A) acquired images over a variety of regions around the world with an imaging geometry different from the one used by the Seasat SAR.

These two exploratory missions were then followed by a series of more sophisticated and operational missions, which brought spaceborne radar imaging to a more mature, although still developing, stage. A series of more sophisticated shuttle imaging radar missions were conducted by the U.S. in 1984 and 1994 [5], leading to multi-spectral and multi-polarization capability. In 2000, an interferometric system was flown on the shuttle to provide global topographic mapping. In the meantime, free-flying, single-frequency systems have been flown by ESA [6], Canada [7], and Japan [8] for Earth observation, and by the U.S. for planetary exploration of Venus [9] and Titan, a moon of Saturn [10].

Spaceborne photography became available in the early 1960's with the advent of the space age. This was followed in the late 1960's and 1970's with the acquisition of multi-spectral visible and infrared (IR) imagery, thermal imagery, and passive microwave imagery. These sensors allowed us to acquire information about the surface by studying its emitted energy in the microwave and IR regions of the spectrum and the reflected energy in the visible and near-IR regions. All these sensors are passive in nature, i.e. they detect the energy that is generated by the sun or the surface.

The SAR imaging sensor provides information about the surface by measuring and mapping the reflected energy in the microwave region, thus extending the capability of sensing the surface properties into a new dimension. In addition, because it uses its own energy and operates at a relatively long wavelength, it acquires surface imagery at all times, i.e. day or night and through cloud cover. Thus it has the unique capability required for continuous monitoring of both static and dynamic surface phenomena.

The imaging resolution of passive sensors is equal to their angular resolution (i.e. observing wavelength over aperture size) multiplied by the range between the sensor and the area

or object being imaged. Thus the size of the resolution element increases linearly with the observing wavelength and sensor altitude, and is inversely proportional to the aperture size. In the optical and IR regions, very high resolution is achievable from orbit with reasonable size apertures because of the short operating wavelength. In the microwave region, the operating wavelength is relatively large, and apertures of many hundreds of meters to many kilometers are required to achieve high resolution of tens of meters or less. This, of course, is impractical at the present time.

The SAR sensor circumvents this limitation by using the ranging and Doppler tracking capability of coherent radar to acquire high-resolution images of the surface from orbital altitudes. Two neighboring targets are separated by their differential time delay and Doppler history, neither of which is a function of the distance to the sensor. Thus the resolution of a SAR system is independent of the sensor altitude. This unique advantage does impose some restriction on the sensor imaging swath, antenna size, and power requirements. The basic properties of spaceborne SAR systems are discussed in Section II and the technological aspects of the sensor are presented in Section III.

Because the SAR uses the Doppler history to achieve high resolution in one of the spatial dimensions, each pixel is generated by processing a large number of successive echoes. This leads to a large number of arithmetic operations in order to generate the image. The development of digital processors for spaceborne SAR data is a very active and challenging research field. This aspect of the SAR system is the subject of Section IV.

Once the image has been formed, a number of post-image-formation processing steps are used to maximize the usefulness of the information in the radar imagery. These include, among

others, radar image registration to topographic data base and multi-spectral visible/IR images and automatic textural analysis. These techniques are addressed in Section IV.

Section V addresses applications of spaceborne SAR data. We present a variety of illustrative examples in the different areas of the earth sciences, geology, oceanography, glaciology, agriculture, and planetary sciences.

In Section VI, we present our opinion of the major challenges in the field of SAR remote sensing and briefly review the development being planned for spaceborne SAR systems during the next decade.

II. SPACEBORNE SAR PRINCIPLE

In the synthetic-aperture technique, the Doppler information in the returned echo is used simultaneously with the time-delay information to generate a high-resolution image of the surface being illuminated by the radar [11], [12], [13], [14], [15]. The radar usually "looks" to one side of the moving platform to eliminate right-left ambiguities, and perpendicular to its line of motion. It transmits a train of short pulses of coherent electromagnetic energy toward the surface. Points equidistant from the radar are located on successive concentric spheres. The intersection of these spheres with a flat surface gives a series of concentric circles centered at the nadir point (see Fig.1). The backscatter echoes from objects along a certain circle will have a well-defined time delay but different Doppler characteristics. Points distributed on coaxial cones, with the flight line as the axis and the radar as the apex, provide identical Doppler shifts of the returned echo but different delays. The intersection of these cones with a flat surface gives a family of hyperbolas (Fig.1). Objects on a specific hyperbola will provide equi-Doppler returns. Thus if the time delay and Doppler information in the returned echoes are processed simultaneously, the surface can be divided into a coordinate system of concentric circles and

coaxial hyperbolas (Fig.1), and each point on the surface can be uniquely identified by a specific time delay and specific Doppler. The brightness that is assigned to a specific pixel (picture-resolution element) in the radar image is proportional to the echo energy contained in the time-delay bin and the Doppler bin which corresponds to the equivalent point on the surface being imaged. The resolution capability of the imaging system is thus dependent on the measurement accuracy of the differential time delay and differential Doppler (or phase) between two neighboring points on the surface.

In actuality, the situation is somewhat more complicated. The radar transmits a pulsed signal in order to obtain the time-delay information. To obtain the Doppler information unambiguously, the echoes from many successive pulses are required with a pulse-repetition frequency (PRF) which meets the Nyquist sampling criterion. Thus, as the moving platform passes over a certain region, the received echoes contain a complete Doppler history and range-change history for each point on the surface that is being illuminated. These complete histories are then processed to identify uniquely each point on the surface and to generate the image. This is why a very large number of operations are required to generate each pixel in the image. Such is not the case with optical sensors. A simplified comparison is that the radar sensor generates the equivalent of a hologram of the surface, and further processing is required to obtain the image.

One unique feature of the synthetic aperture- imaging radar is that its resolution capability is independent of the platform altitude. This is a result of the fact that the image is formed by using the Doppler history and the differential time delays, none of which is a function of the range from the radar to the surface. This unique capability allows the acquisition of high-

resolution images from satellite altitude as long as the received echo has sufficient strength above the noise level.

Another unique feature of synthetic aperture radar is that the transmitted and received signals are handled coherently, i.e., both amplitude and phase are fully preserved. This allows the use of phase information in a very powerful way, particularly in recently developed interferometric systems.

In the design of SAR systems a number of factors need to be taken into consideration [15]. The transmitted pulses have to be carefully timed to keep the receiving echoes from arriving at the antenna at the same time as later transmitted pulses. At the same time, the pulse repetition frequency (PRF) must be high enough to fully sample the Doppler spectrum spread. These so-called "ambiguity" criteria lead to the conclusion that the antenna area A must be larger than a minimum given by [5b]:

$$A > \frac{4v\ \lambda h}{c}\ \frac{\sin\ \phi}{\cos^2 \phi}$$

where v is the platform velocity, λ is the radar signal wavelength, h is the platform altitude, ϕ is the look angle and c is the speed of light. In addition, full consideration is required of the Earth (or planet) surface motion due to the planet rotation, motion of the target within the illumination beam during integration, the change of the distance to the target while it is in view of the sensor, and the coherent nature of the wave-surface interaction which leads to speckle noise, similar to the granularity observed when a surface is illuminated by a laser beam.

All of the above factors are traded off during the design of the system with the scientific and application requirements such as resolution, coverage, illumination geometry and sensitivity.

One of the most exciting developments in the last five years is the use of spaceborne SARs in an interferometric configuration [16, 17, 18, 19]. In this case, two spatially separated antennae (Fig. 2) are simultaneously used either at transmission or reception or at both. An interesting variation is to use a single antenna system but combine data from two slightly displaced orbital passes to simulate an effective interferometer (Fig. 2). This interferometeric technique provides a third independent measurement (i.e., phase difference of the signals received at the two antennas, in addition to time delay and Doppler history) which effectively enables one to obtain the target location in three dimensions. This allows 3-D imaging of the surface and therefore provides perspective views of the surface (Fig. 3). This exciting technique has been used experimentally to derive topographic maps and was used operationally on a shuttle mission in February 2000 to generate global topographic maps of the Earth's land surface, with horizontal posting of 30m and height resolution of better than 10m [20]. This Shuttle Radar Topography mission (SRTM) is described in later sections.

Another derivative of multi-path radar interferometry is that where topography is well known, the third independent measurement can be used to derive very subtle surface changes and displacement that can result from earthquakes or volcanic deformation [21, 22, 23]. This new capability of mapping surface motion due to tectonic or volcanic activity is becoming a very important geophysical tool to study the Earth's dynamic.

III. SPACEBORNE SAR SENSORS

A SAR system can be divided into five major elements (Fig. 4). The antenna is the interface between the on-board RF electronics and free space. It radiates the electromagnetic energy toward the object to be sensed, and it collects the back-scattered energy. The RF electronics consist of the transmitter subsystem, which generates the RF signal, and the receiver

subsystem, which detects the returned energy and converts it to a form which can be handled by the data handling element. This element, in turn, reformats the data and either sends it to an on-board digital recorder (in the case of shuttle-borne systems) or sends it to a high capacity link for transmission to and recording on the ground (in the case of free flyers and planetary systems). This record contains what is commonly called the "signal data." These first three elements are referred to as the "SAR sensor."

The details of SAR sensor systems which have been flown in the 70's, 80's and 90's can be found in numerous open literature papers [24]. In this section, we will briefly discuss some of the special features that differentiate these different systems.

The Seasat (1978), SiR-A (1981) and SiR-B (1984) are fundamentally similar systems. The antenna was a planar array system about 2 x 10m in size. The system operated at L-band (1.275 Ghz) using a 1 kw solid state transmitter system with a bandwidth of about 6 to 20 Mhz, providing surface resolution of about 25m over a swath width of about 50 to 100 km. The Japanese radar system (JERS-1, 1992) used a very similar approach.

The SiR-C/XSAR radar system (1994) made a major advance by operating at three frequencies (L-band at 1.25 Ghz, C-band at 5.3 Ghz, and X-band at 9.6 Ghz), thus providing for the first time, spaceborne radar images in "color." In addition, the L- and C-band channels, developed by the U.S., used a distributed planar array approach where hundreds of solid state transmitter/receiver elements were spread across the antenna surface, providing high redundancy in the system. In addition, the system provided full polarization capability. The X-band system, developed by a German/Italian team, provided the first spaceborne X-band radar images. The SiR-C/XSAR system was flown twice in 1994, providing seasonal multi-spectral images at resolutions between 8 and 25m of a significant fraction of the Earth's surface. In addition, this

system demonstrated two operational modes. The SCANSAR mode, where the beam is electronically stepped across track during the synthetic aperture period, allowing a significant increase in the swath width, and therefore coverage at the expense of resolution; and the SPOTLIGHT mode, where the boresight angle was electronically skewed as the shuttle flew by to increase the dwell time on a specific area, allowing significant increase in the resolution (down to 1.5m in azimuth) at the expense of coverage. The SiR-C/XSAR was also used to demonstrate repeat track interferometry.

The SRTM (2000) system effectively uses the SiR-C/XSAR hardware but with the addition of a 60m deployable boom, with a second C-band and X-band receiving antenna. This interferometric system mapped the Earth's land surface between 60° north and 56° south in a single 11-day shuttle mission, and generated digital topographic maps of the mapped area, with 30m horizontal posting and 10m vertical resolution. This provided, for the first time, digital topographic maps of almost 80% of the Earth's surface in a digital format, referenced to a single-frame system.

The European (ERS-1, 1991; ERS-2, 1995) and Canadian (Radarsat 1995) systems are free flying operational systems that operate at one frequency (C-band) and provide global continuous coverage at resolutions of 10 to 25 meters. They use planar or waveguide array antenna and traveling wave tube amplifiers.

The Magellan radar system was flown in 1989 [9] and provided, for the first time, a global image of the cloud hidden surface of Venus. Because of the tight mass limitations on planetary missions, the Magellan SAR shared the same 3.7-meter parabolic dish antenna with the telecommunications system. During part of the orbit around periapsis, the spacecraft pointed the antenna toward Venus' surface and acquired SAR data, using an S-band, 20-watt, solid state

transmitter. This data was recorded and played back to Earth during the part of the orbit around apoapsis, when the spacecraft pointed the same antenna toward Earth. This antenna-pointing dance took place on each orbit for the multi-year lifetime of the mission. This mission provided 98% coverage of the surface at a resolution of about 120 meters. The same system was used for altimetric and radiometric measurements.

The same basic approach is being used on the Cassini radar, which was launched in 1997 and will go into orbit around Saturn in 2004 [10]. During a 4-year period, the Cassini spacecraft will fly by the Moon Titan between 40 and 50 times. During some of the flybys, an on-board Ku-band (13.8 Ghz) radar system will use the 4m telecommunication antenna to acquire SAR, altimetry and radiometry data of the haze-covered surface. This system, jointly developed by the U.S. and Italy, uses a TWT for signal generation and a 5-beam feed network to allow wide coverage of the surface. Because of the limited number of flybys, it is expected that only about 20% of the surface will be imaged at better than 1 km, with global coverage achieved only in the radiometric mode, with resolution of many 10's to 100 km.

IV. IMAGE PROCESSING

The first step in radar image processing is to form an image from the raw echoes. The SAR image formation process is to use coherent phase information in an array of radar echoes to synthesize an effective antenna aperture which is much larger than the size of the physical antenna. This approach enables high-spatial-resolution radar images to be attained with a practical-size antenna. Digital processing for SAR image formation involves sampled and quantized SAR echo data and represents a numerical evaluation of synthetic-aperture beam-formation process. A large number of arithmetic computations are involved. The process, nevertheless, can be very accurate in representing the

radiometric reflectivity of the target surface being imaged. The inherent flexibility in a sequential execution of digital SAR processing functions also allows users to extract special information such as Doppler spectra and pixel phases at various intermediate stages of the SAR correlation process.

The arithmetic computation requirement for digital SAR image formation corresponds to the product of the number of computations involved to produce an output pixel and the pixel-throughput rate required for the system. For SAR image formation in real time, both the pixel rate and the per-pixel computation increase with the resolution capability. For a typical spaceborne SAR operating at L-band, such as Seasat SAR, the computation rate required for real-time processing exceeds 10^9 operations/s.

The large number of arithmetic computations characterizes one part of the digital SAR correlation task. The numerical nature of the digital correlation process calls for the formulation of an accurate mathematical procedure, which is often referred to as the SAR correlation algorithm, to manipulate the sampled echo signals to accomplish the SAR correlation process. Design of this procedure is a two-step process. The first step involves an accurate modeling of the SAR response to a point target as well as a continuous field of reflecting targets. This modeling is required to formulate an inversion process and to provide all the necessary functions for reconstructing the target scene from the received echo signals. The model is also essential in evaluating the performance of a SAR System with respect to its attainable limit. The second step is to implement the processing functions of the SAR image reconstruction process in a clearly defined, mathematical computation procedure. Because digital processing is a sequential procedure, a computationally efficient algorithm often implies savings in computing time or hardware logics and may dictate the selection of a specialized hardware architecture. Besides the

computational efficiency of the algorithm, the related costs of software and hardware implementation and maintainability of the system are all of practical concern.

Because of the high rate of computation needed, digital processors for spaceborne SAR became operational only in the last decade and the development of more capable systems is a field of active research particularly when it involves the need for real time processing and advanced information extraction such as in interferometry. Excellent textbooks on the subject have been recently published [25, 26].

Once the raw data has been transformed to an image, a number of post processing steps can be undertaken to utilize the data. These include: 1) geometric calibration to allow projection of the data on predetermined geographic grids, 2) registration to other data sets such as topographic maps, land use data base, visible/IR images etc..., 3) radiometric calibration to extract quantitative backscatter cross section, and then subsequently physical parameters such as soil moisture, vegetation thickness, surface roughness, etc..., 4) image texture which could be related to surface properties.

V. IMAGE INTERPRETATION AND APPLICATIONS

The tone of the radar image is a representation of the surface backscatter cross section, which in turn is a function of the surface slope, roughness, dielectric constant and volumetric structure of the surface cover or near subsurface. In addition any surface motion will affect the Doppler signature.

The interpretation of SAR images and raw data is based on three types of information: 1) geometric patterns, forms, and shapes; 2) image tone and texture, and associated changes with frequency and polarization when multispectral polarimetric radars are used; 3) coherency

properties such as Doppler shift and phase changes particularly in the case of interferometric configurations.

Figure 5 shows two well known coastal urban areas, San Francisco and Hong Kong. The ocean surface is dark blue/black. Ocean vessels, bridges, airport runways, and major highways are easily visible. Urban areas can be easily separated from non-developed areas allowing city planners to regularly monitor urban expansion, particularly in developing countries.

Figure 6 illustrates land use in agricultural regions. This figure was taken in Central Ukraine, southeast of Kiev. Cultivated fields can be easily delineated and differentiated from non-cultivated and urban areas along the Dnieper River. Future research should allow the classification and monitoring of the vegetation type and surface moisture level based on multispectral and multipolarimetric signature of different fields.

Figure 7 shows striking geologic folds in the layered rocks in the Moroccan Atlas mountains near the town of Rissani. Some of the folded structures have been disrupted due to fault movement and earthquakes.

Figure 8 provides an illustrative example of two volcanic regions: The island of Maui and Kamchatka penninsula. In the Maui image, the light blue and yellow areas in the center of the island are sugar cane fields. The West Maui volcano, in the lower left is considered extinct. The East Maui volcano at the top right features the spectacular Haleakalu crater with numerous volcanic cones and lava flows on the floor of the crater. The Kliuchevskoi volcano in Kamchatka is a presently active volcano. Lava flows can be easily seen particularly on the left of the image along the flanks of the volcano. Repetitive coverage during eruptive episodes allows monitoring of lava motion even through cloud and plume cover.

By combining radar images with interferometric radar data, three dimensional images and perspective views can be generated as illustrated in Fig. 9 of the Long Valley in California.

Multipath radar coverage, before and after an earthquake, can be coherently combined to derive surface motion due to an earthquake as shown in Fig. 10. This allows new insight in understanding earthquake physics and the effect of the geologic environment on the surface displacement. Hopefully this would lead to a better understanding of the Earth tectonic activities and possibly their prediction.

Figure 11 provides a dramatic illustration of the penetration capability of long wavelength radars. It shows visible (top) and radar (bottom) images of the Nile region near the fourth cataract in Sudan. The lower image shows, in bright white, an old course of the river which is presently covered by a sand sheet, and is invisible on visible imagery. Surface measurements in Western Egypt and the Mojave desert lead us to believe that subsurface penetration of up to 3 to 5 meters is possible in arid regions.

Figure 12 shows oil slicks (dark streak) in the Arabian Sea as well as the drilling platforms (bright white spots). This illustrates the ability of radar sensors to be used for oil spills monitoring. In addition, ocean swells and internal waves (top center) are clearly visible. This allows monitoring of ocean surface waves on an operational basis.

Figure 13 and 14 shows an example of the topographic data and resulting perspective views acquired with the SRTM mission.

VI. FUTURE DEVELOPMENTS

As described earlier, the last two decades of the 20th century saw dramatic advances in spaceborne imaging radar. The first decade of the 21st century will also see significant advances in transforming this type of sensor data to operational use for Earth observation, in wider

application to planetary exploration and in technological development, making this type of sensor easily affordable.

Present systems emphasize either global continuous coverage from a free flyer but with limited spectral capability, or sophisticated multi-spectral, multi-polarization and/or interferometric capability but from limited duration flights on the shuttle. In the next decade, it is envisioned that these capabilities will be merged into multi-parameter, free-flying systems, which will provide direct access to users with small receiving stations. These systems will provide real-time data that will allow tracking of oil spills, flood monitoring, earthquake damage assessment, volcanic eruption prediction, navigation in polar regions, land cover assessment, etc. In addition, it is envisioned that systems developed by different organizations (NASA, ESA, Japan, Canada, etc.) would follow agreed-upon standards so the data can be acquired from different systems to extend coverage and timeliness, or simultaneously from different systems to achieve interferometric capabilities.

In order to achieve fully operational capability, the cost of SAR systems and associated processors needs to be reduced significantly. A number of areas hold particular potential. Large inflatable antennae could allow significant reduction in weight and volume at launch, thus driving down the requirements on the launch vehicle with associated cost reduction. Electronics miniaturization and the integration of digital and analogue functions on single chips would lead to significant reduction in weight, volume and power requirements. Finally, on-board processing would reduce the link requirements and make wider access of real time data easier.

Significant new applications in the planetary exploration area are also planned. The capability of radar waves to penetrate through low loss surface covers such as sand and eolian deposits is generating interest in mapping the surface of Mars, with the objective of detecting old

drainage channels which are now covered by a sand sheet. The ability of very low frequency (few tens of Mhz) to deeply penetrate ice sheets and dry surfaces has led to strong interest in including a radar-sounder as part of the payload of the ESA Mars Express (2003) for sounding the martian surface down to 1 km with the objective of detecting a potential water table, and as part of the U.S. Europa Orbiter (2003) for sounding the surface ice cover down to many tens of kilometers with the objective of detecting the presence of a subsurface ocean.

Finally, new SAR configurations might be demonstrated. One possibility is to use SAR orbiting receivers on a different platform than the transmitter. This bi-static configuration might provide new information about the surface. It will also open the possibility of using available resources such as the surface reflection of GPS signals or telecommunication satellite signals to generate bistatic images.

ACKNOWLEDGMENT

The research described in this paper was carried out at Jet Propulsion Laboratory, California Institute of Technology, under a contract with the National Aeronautics and Space Administration.

REFERENCES

[1] Born, G., Dunne, J. A., and Lowe, D. B., "SEASAT Mission Overview," *Science*, Vol. 24, 1979, pp. 1405-1406.

[2] Elachi, C., "Spaceborne Imaging Radar: Geologic and Oceanographic Applications," *Science*, Vol. 209, 1980, pp. 1073-1082.

[3] Elachi, C. "Wave Patterns Across the North Atlantic on September 28, 1974 from Airborne Radar Imagery," *J. Geophys. Res.*, Vol. 81, May 20, 1976, pp. 2655-2656.

[4] Elachi, C., Brown, W. E., Cimino, J. B., Evans, D. L., Ford, J. P., Saunders, R. S., Breed, C., Masursky, H., McCauley, J. F., Shaber, G., Dellwig, L., England, A., MacDonald, H. Martinakaye, P., Sabins, F., "The Shuttle Imaging Radar (SIR-A): Preliminary Results," *Science*, Vol. 218, 1982, pp. 996-1003.

[5] Elachi, C. "Spaceborne Synthetic Aperture Imaging Radars: Applications, Techniques, And Technology," *Proc. IEEE*, Vol. 70, 1982, pp. 1179-1209.

[6] Attema, E. W. P., "The Active Microwave Instrument On-board the ERS-1 Satellite," *Proc. IEEE*, Vol. 79, 1991, pp. 791-799.

[7] Luscombe, A. P., Ferguson, I, Shepherd, N., Zimcik, D. G., and Naraine, P., "The RadarSAT Synthetic Aperture Radar Development, "*Canadian Journal of Remote Sensing*," Vol. 19, 1993, pp. 298-310.

[8] Nemoto, Y. Nishino, H., Ono, M., Mizutamari, H., Nishikawa, K., Tanaka, K., "Japanese Earth Resources Satellite-1 Synthetic Aperture Radar," *Proc. IEEE*, Vol. 79, 1991, pp. 800-808.

[9] Johnson, W. T. K., "Magellan Imaging Radar Mission to Venus," *Proc. IEEE*, Vol. 79, 1991, pp. 777-790.

[10] Elachi, C., Allison, M. D., Borgarelli, L., Encrenaz, P., Im, E., Janssen, M. A., Johnson, W. T. K., Kirk, R. L., Lorenz, R. D., Lunine, J. I., Muhleman, D. O., Ostro, S. J., Picardi, G., Posa, F., Rapley, C. G., Roth, L. E., Seu, R., Soderblom, L. A., Vetrella, S., Wall, S. D., Wood, C. A., and Zebker, H. A., "The Cassini Titan Radar Mapper," *Space Science Review*, in press, 2000.

[11] Brown, W. M. and Porcello, L. J., "An Introduction to Synthetic Aperture Radar," *IEEE Spectrum*, Vol. 6, 1969, pp. 52-62.

[12] Elachi, C., "Radar Images of the Earth," *Scientific American*, Dec. 1982, pp. 54-61.

[13] Harger, R. O. *Synthetic Aperture Radar Systems: Theory and Design*, Academic Press, New York, 1970.

[14] Kovaly, J. J., *Synthetic Aperture Radar*, Artech House, Dedham, MA, 1976.

[15] Elachi, C., "Spaceborne Radar Remote Sensing: Applications and Techniques," IEEE press, 1988.

[16] Graham, L. C., "Synthetic Interferometric Radar for Topographic Mapping," *Proc. IEEE*, Vol. 62, No. 6, 1974, pp. 763-768.

[17] Zebker, H. A. and Goldstein, R. M., "Topographic Mapping from Interferometric SAR Observations," *J. Geophys. Res.*, 91, 1986, pp. 4993-4999.

[18] Li, F. and Goldstein, R. M., "Studies of Multibaseline Spaceborne Interferometric Synthetic Aperture Radars," IEEE Trans. *IEEE Trans. Geosci. Remote Sens.*, GRS-28, 1990, pp. 88-97.

[19] Rosen, P. A.., Hensley, S., Joughin, I. R., Li, F. K., Madsen, S. N., Rodriguez, E., Goldstein, R. M., "Synthetic Aperture Radar Interferometry," *Proc. IEEE*, Vol. 88, No. 3, March 2000.

[20] Hilland, J. E., Stuhr, F. V., Freeman, A., Imel, D., Shen, Y., Jordan, R. and Caro, E., Future NASA Spaceborne SAR Missions, *IEEE-AES Systems Magazine*, Vol. 13, No. 11, November 1998.

[21] Massonnet, D., Rossi, M., Carmona, C., Adragna, F., Peltzer, G., Fiegl, K., and Rabaute, T., "The Displacement Field of the Landers Earthquake Mapped by Radar Interferometry," *Nature*, Vol. 364, 1993, pp. 138-142.

[22] Peltzer, G. and Rosen, P. "Surface Displacement of the 17 May 1993 Eureka Valley, California, Earthquake Observed by SAR Interferometry," *Science*, Vol. 268, 1995, pp. 1333-1336.

[23] Peltzer, G., Crampe, F., King, G., "Evidence of Non-linear Elasticity of the Crest from the 7.6 Manyi (Tibet) Earthquake," Science, Vol. 286, 1999, pp. 272-276.

[24] Kim, Y., Stuhr, F., van Zyl, J., Rosen, P., Freeman, A., Johnson, W., Jordan, R., Caro, E., Shen, Y., "Achievements in the Development of Spaceborne Imaging Radar," *IEEE AES Magazine*, in press, 2000.

[25] Franceschetti, G. and Lanari, R., "Synthetic Aperture Radar Processing," CRC Press, 1999.

[26] Curlander, J. and McDonough, R., "Synthetic Aperture Radar: Systems and Signal Processing," John Wiley and Sons, 1991.

Fig. 1: Coordinate system for SAR image formation. A set of circles and hyperbolas define the equirange and equiDoppler lines, respectively.

Fig. 2: Two possible configurations for radar interferometry: a) data are acquired with two antennas connected by a beam of length d; b) data are acquired with one antenna used on two flight passes separated by a distance d

Fig. 3: Perspective view of the Karakax valley in Tibet created by combining two radar images using interferometry

Fig. 4: Elements of a radar system

Fig. 5a: SIR-C/XSAR images of San Francisco urban areas

Fig. 5b: SIR-C/XSAR images of Hong Kong urban areas

Fig. 6: SIR-C/XSAR image of an agricultural area in Central Ukraine, along the Dnieper river where it intersects with the Volchya river.

Fig. 7: SIR-C/XSAR image of folded structures on the eastern flanks of the Atlas mountains in Morocco, near the town of Rissani

Fig. 8a: SIR-C/XSAR image of the island of Maui

Fig. 8b: SIR-C/XSAR image of the Kliuchevskoi volcanic region in central Kamchutka

Fig. 9: SIR-C/XSAR regular radar image (top left) and interferometric image (top right) of Long Valley, California. At bottom left, is the topographic data derived from the interferometric data and rotated to place north at top. At bottom right is the resulting perspective image of the region.

Fig. 10: Displacement from the 7.1 magnitude Hector Mine Earthquake in California (Oct. 16, 1999) as derived from two ERS-2 radar images taken before (Sept. 15, 1999) and after (Oct. 20, 1999) the earthquake [Courtesy of G. Peltzer, JPL].

Fig. 11: Photographic (top) and SIR-C/XSAR image of the Nile near the fourth cataract in Sudan

Fig. 12: SIR-C/XSAR image of an oil producing region in the Arabian Sea, showing oil slicks (dark areas) and oil platforms and slopes (bright points).

Fig. 13: a) SRTM Interferometric fringes acquired over the island of Oahu which reflect the surface topographic contours of the Island; b) Landsat images/SRTM derived topography are used to generate a perspective view of Honolulu and the surrounding region.

Fig. 14: Perspective view of Pasadena and the San Gabriel Mountains derived from SRTM generated topography data, landsat image color and airborne photography. The Rose Bowl is clearly visible to the left of the image.

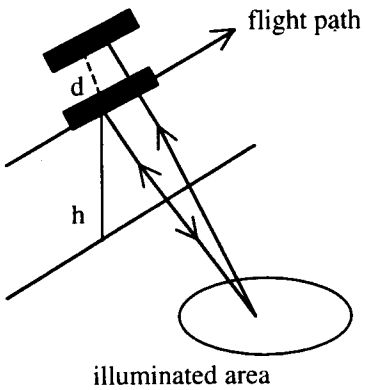
flight path
d
h
illuminated area

(a)

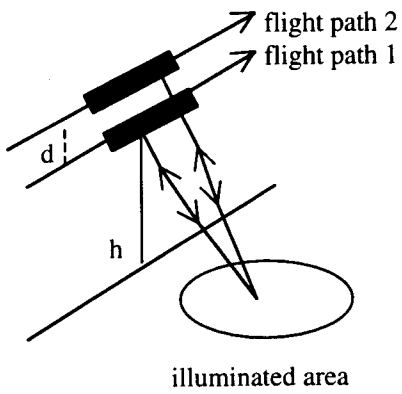
flight path 2
flight path 1
d
h
illuminated area

(b)

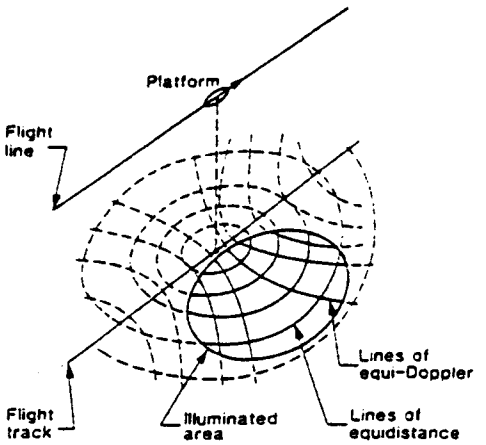
Platform
Flight line
Flight track
Illuminated area
Lines of equi-Doppler
Lines of equidistance

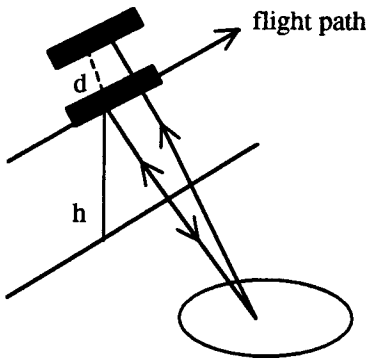
flight path
d
h
illuminated area

(a)

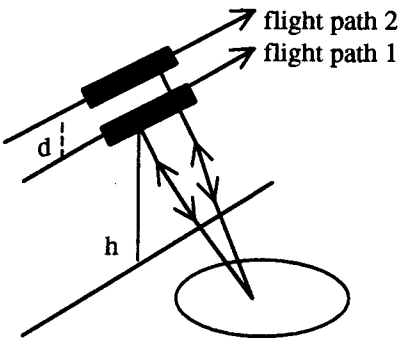
flight path 2
flight path 1
d
h
illuminated area

(b)

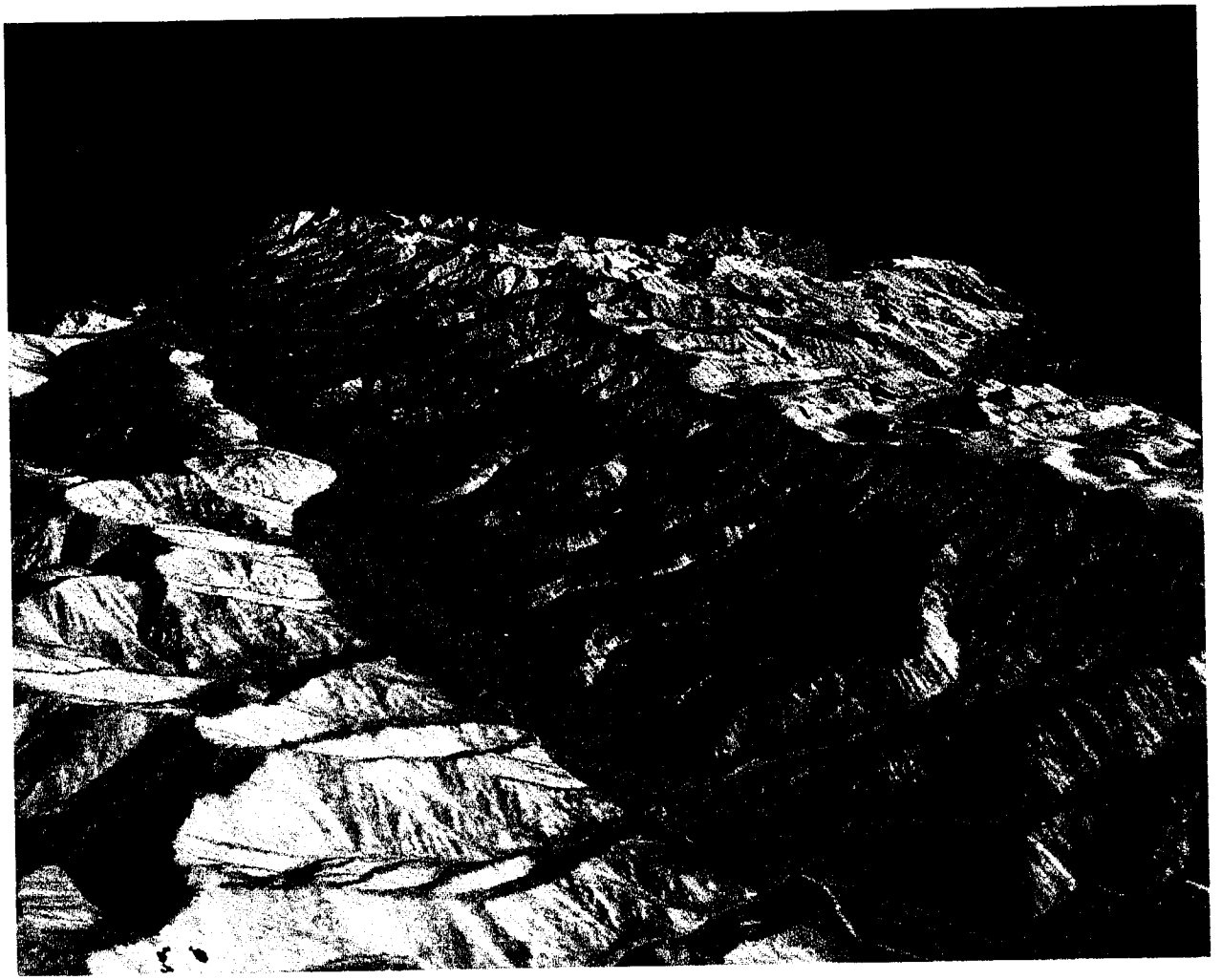

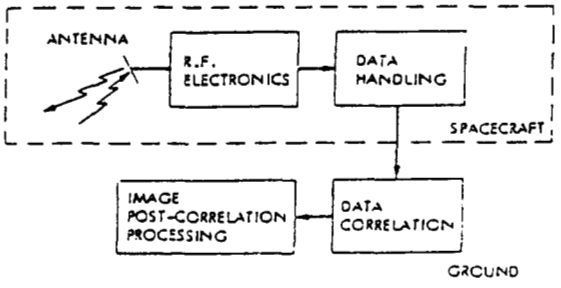
ANTENNA
R.F.
ELECTRONICS
DATA
HANDLING
SPACECRAFT
IMAGE
POST-CORRELATION
PROCESSING
DATA
CORRELATION
GROUND

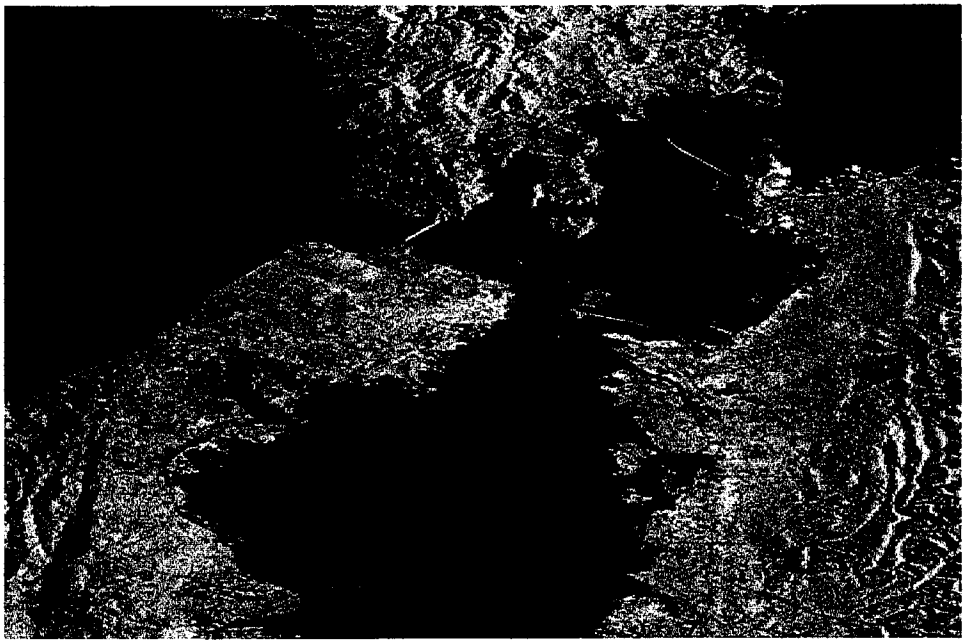

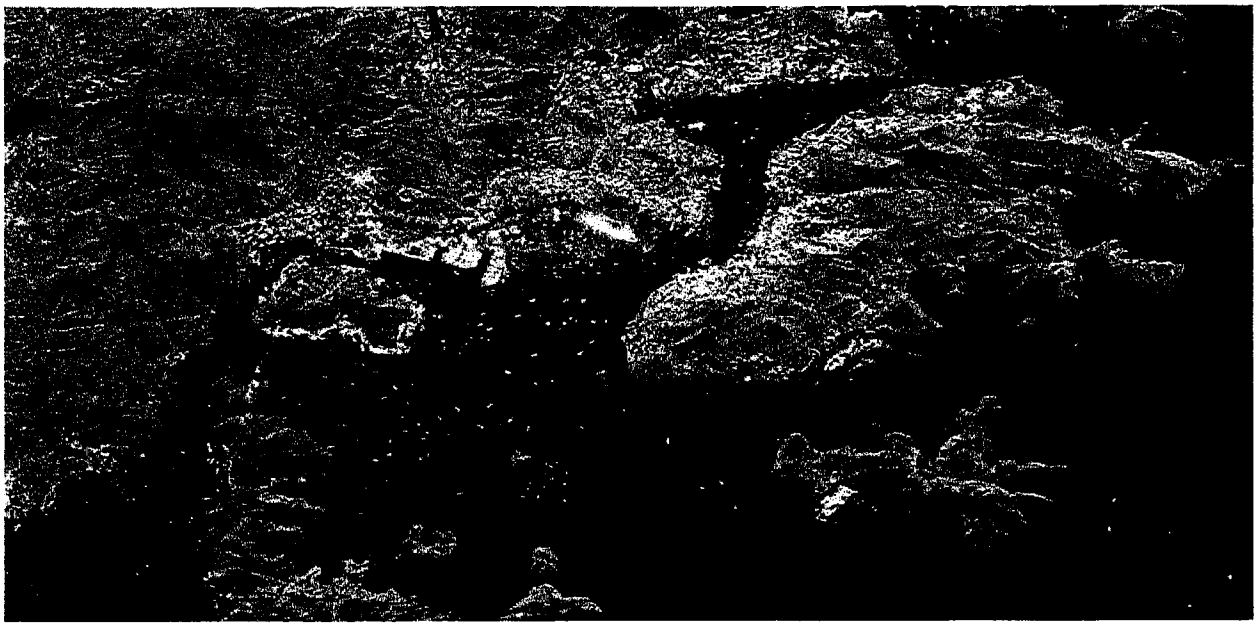

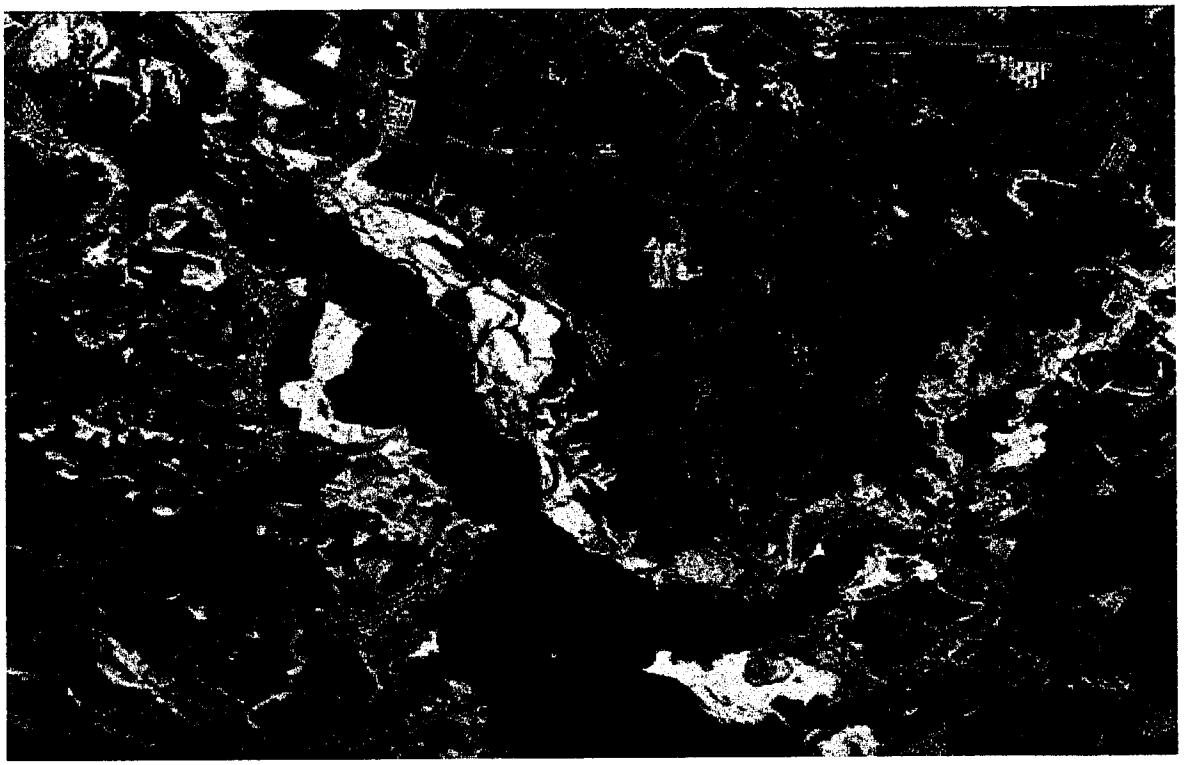

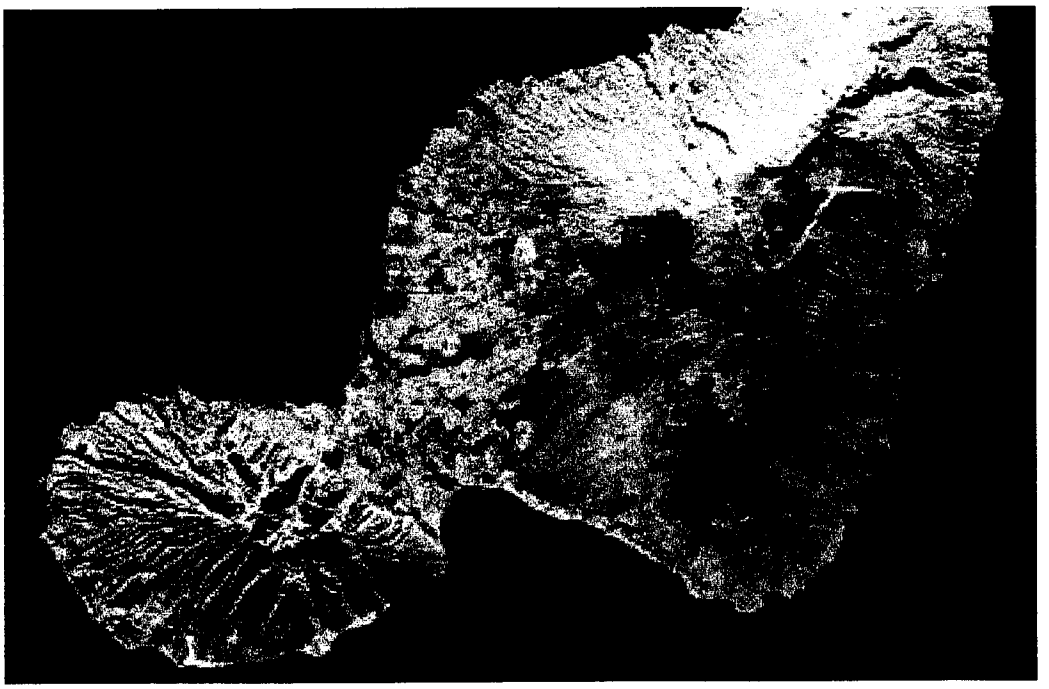

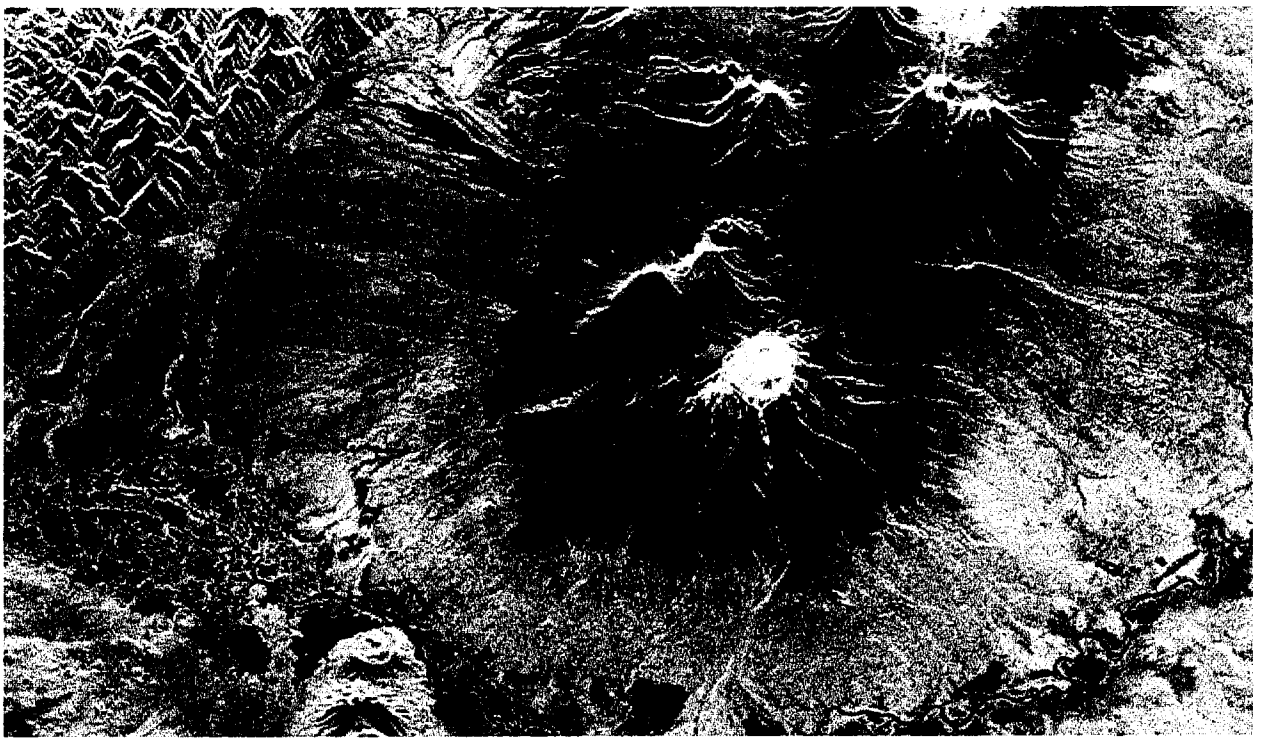

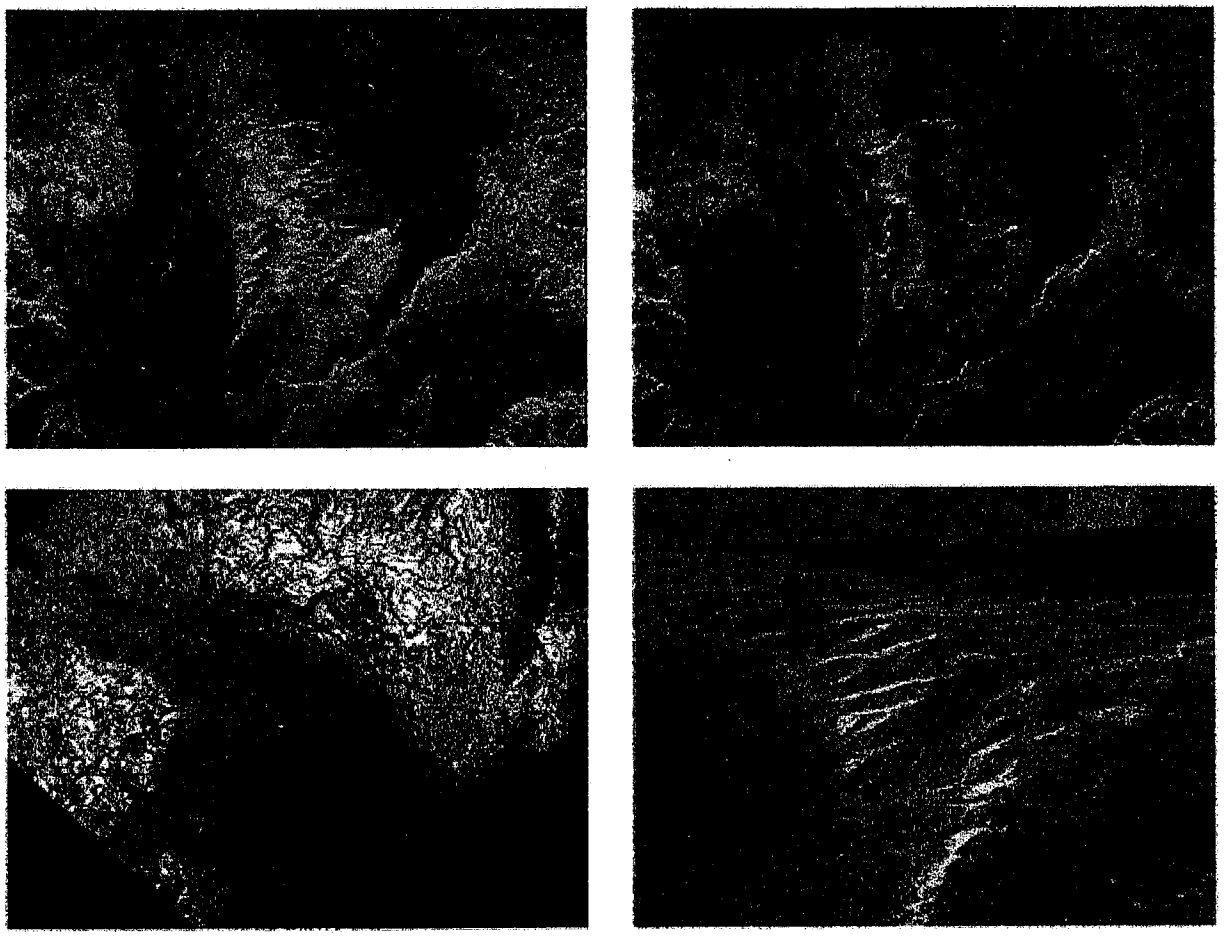

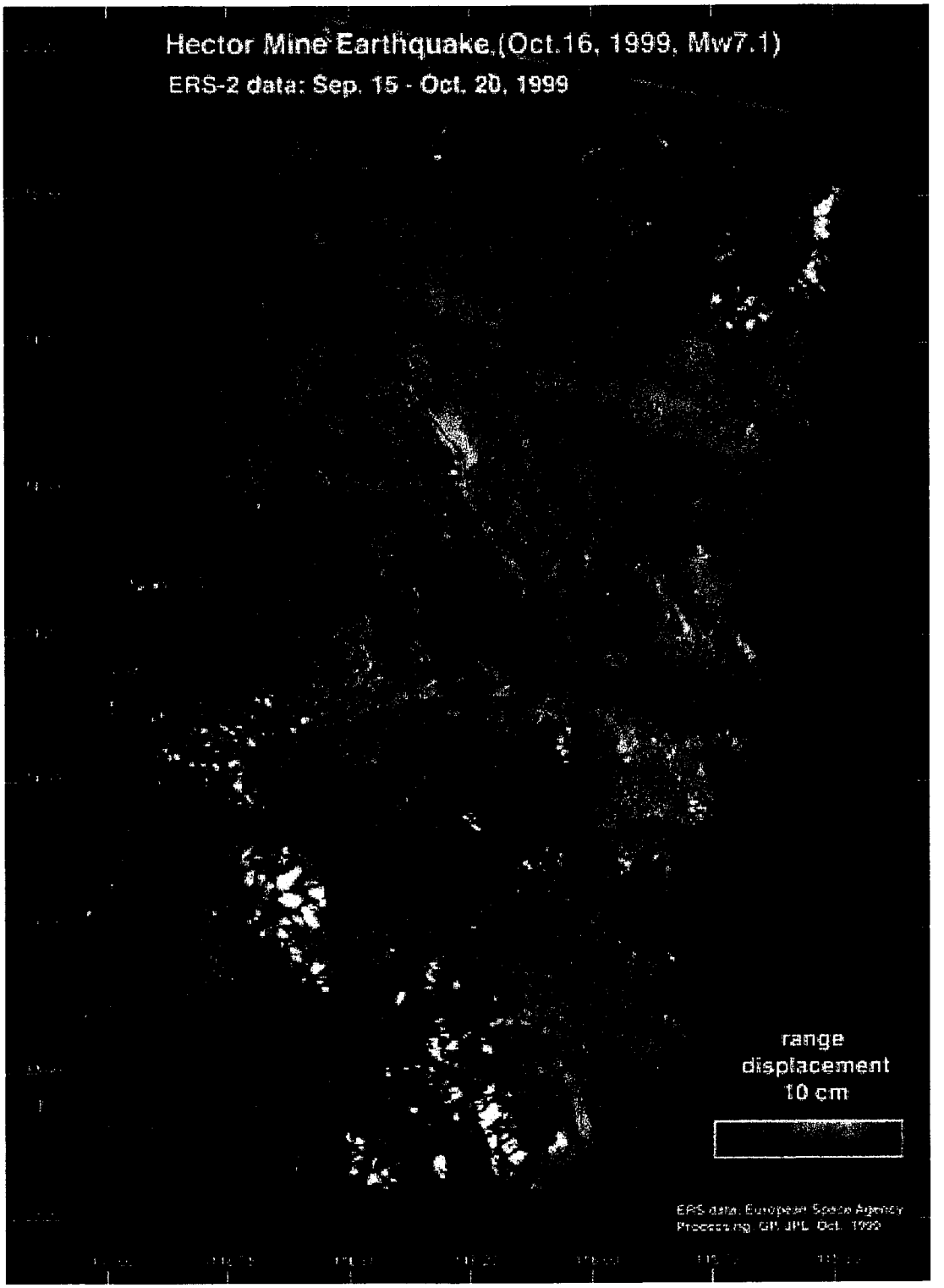
Hector Mine Earthquake,(Oct.16, 1999, Mw7.1)
ERS-2 data: Sep. 15 - Oct. 20, 1999
range
displacement
10 cm
ERS data: European Space Agency
Processing: GPL JPL Oct. 1999

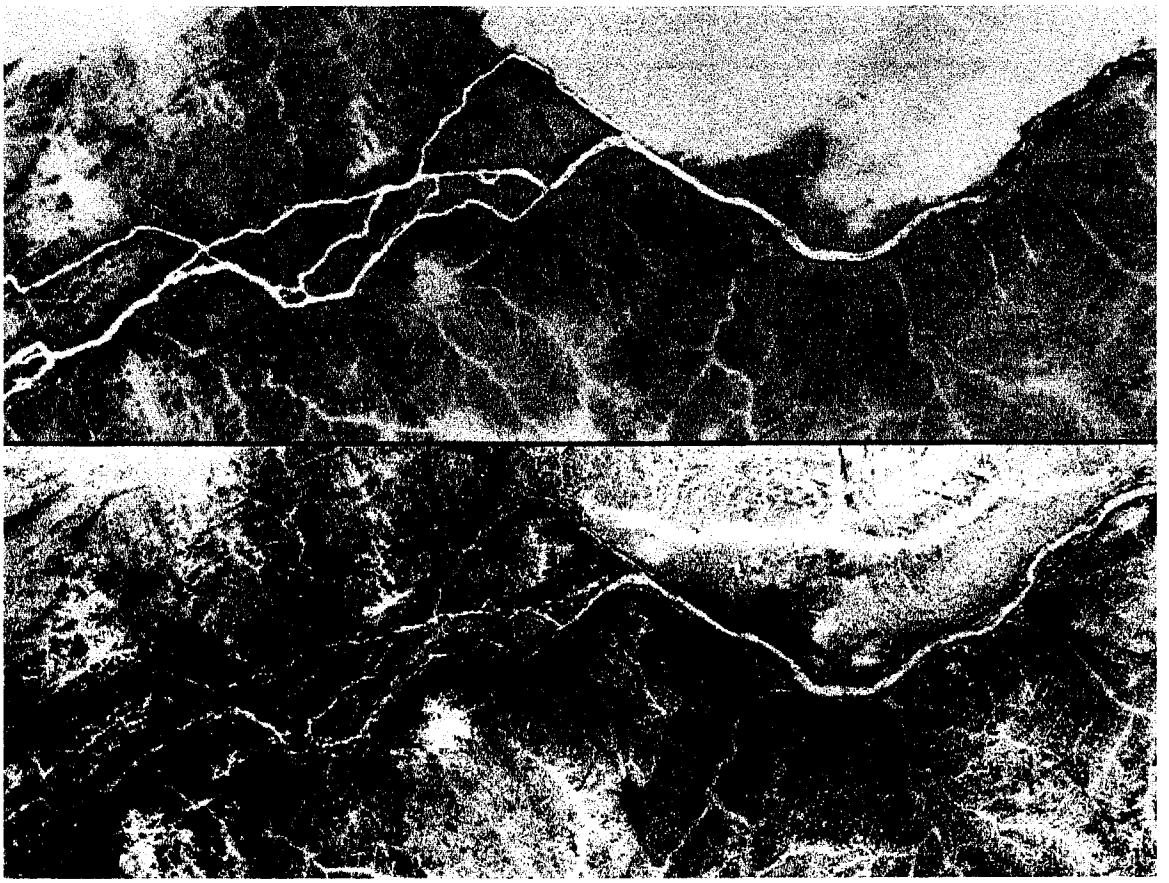

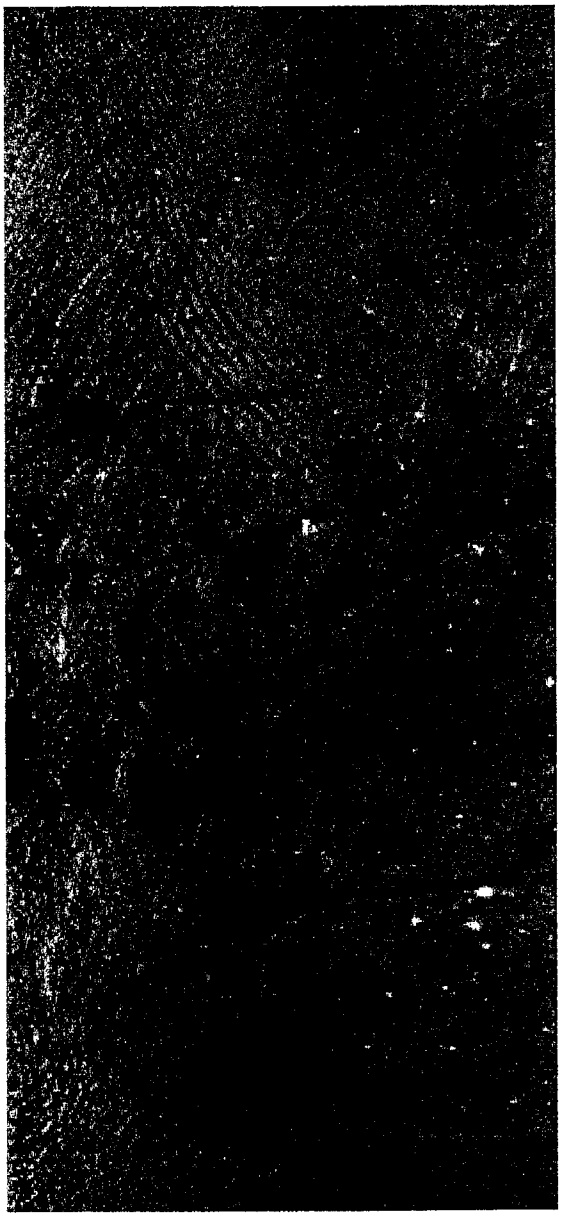

Elachi Fig. 12

Elachi. Fig. 13

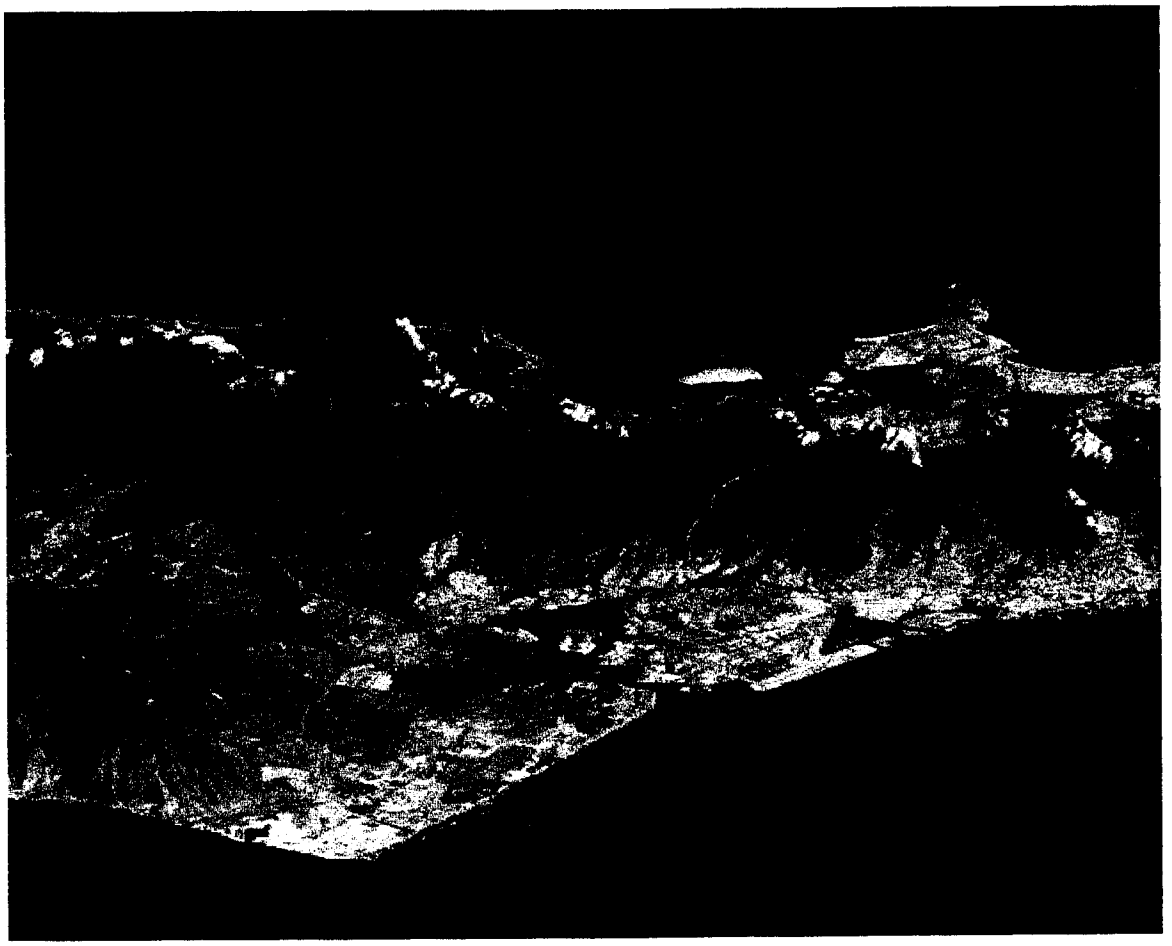

Elachi fig. 13b

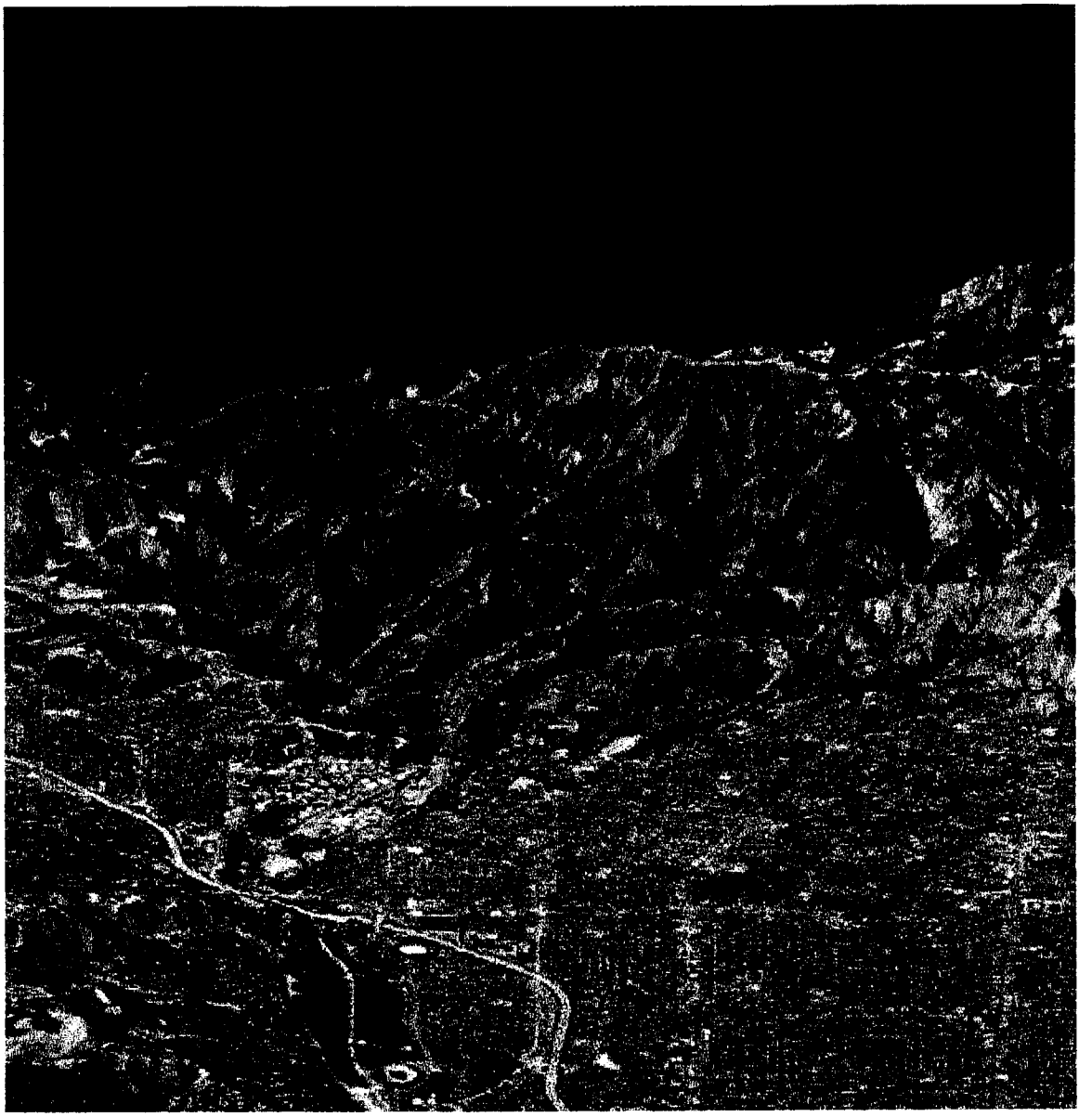

Mach. Fig. 14